communications earth & environment

ARTICLE

https://doi.org/10.1038/s43247-022-00618-z OPEN

# The unexpected radiative impact of the Hunga Tonga eruption of 15th January 2022

P. Sellitto[1,2✉], A. Podglajen[3], R. Belhadji[1], M. Boichu[4], E. Carboni[5], J. Cuesta[1], C. Duchamp[3], C. Kloss[6], R. Siddans[5], N. Bègue[7], L. Blarel[4], F. Jegou[6], S. Khaykin[8], J. -B. Renard[6] & B. Legras[3]

The underwater Hunga Tonga-Hunga Ha-apai volcano erupted in the early hours of 15th January 2022, and injected volcanic gases and aerosols to over 50 km altitude. Here we synthesise satellite, ground-based, in situ and radiosonde observations of the eruption to investigate the strength of the stratospheric aerosol and water vapour perturbations in the initial weeks after the eruption and we quantify the net radiative impact across the two species using offline radiative transfer modelling. We find that the Hunga Tonga-Hunga Ha-apai eruption produced the largest global perturbation of stratospheric aerosols since the Pinatubo eruption in 1991 and the largest perturbation of stratospheric water vapour observed in the satellite era. Immediately after the eruption, water vapour radiative cooling dominated the local stratospheric heating/cooling rates, while at the top-of-the-atmosphere and surface, volcanic aerosol cooling dominated the radiative forcing. However, after two weeks, due to dispersion/dilution, water vapour heating started to dominate the top-of-the-atmosphere radiative forcing, leading to a net warming of the climate system.

[1] Univ. Paris-Est Créteil and Université de Paris-Cité, CNRS, Laboratoire Interuniversitaire des Systèmes Atmosphériques (LISA-IPSL), Institut Pierre Simon Laplace, Créteil, France. [2] Istituto Nazionale di Geofisica e Vulcanologia, Osservatorio Etneo, Catania, Italy. [3] Laboratoire de Météorologie Dynamique (LMD-IPSL), UMR CNRS 8539, ENS-PSL, École Polytechnique, Sorbonne Université, Institut Pierre Simon Laplace, Paris, France. [4] Univ. Lille, CNRS, UMR 8518—LOA—Laboratoire d'Optique Atmosphérique, 59000 Lille, France. [5] UK Research and Innovation, Science and Technology Facilities Council, Rutherford Appleton Laboratory, Chilton, UK. [6] Laboratoire de Physique de l'Environnement et de l'Espace, CNRS UMR 7328, Université d'Orléans, Orléans, France. [7] Laboratoire de l'Atmosphère et des Cyclones, UMR 8105 CNRS, Université de la Réunion, Météo-France, Saint-Denis de La Réunion, France. [8] Laboratoire Atmosphères, Milieux, Observations Spatiales (LATMOS-IPSL), UMR CNRS 8190, Institut Pierre Simon Laplace, Sorbonne Univ./UVSQ, Guyancourt, France. ✉email: pasquale.sellitto@lisa.ipsl.fr

Major volcanic eruptions emit gas and aerosol pollutants into the stratosphere, which have substantial impact on the atmospheric radiative balance and the climate system[1–3]. After a phase of volcanic unrest starting from end December 2021, and strong explosions on 14th January 2022, removing the aerial part of the volcano, the submarine Hunga Tonga–Hunga Ha'apai (HT) volcano (20.57°S, 175.38°W) violently erupted on 15th January 2022, with a series of explosions from approximately 04:00 to 05:00 UTC[4,5]. The eruption produced tsunamis over a large area of the Pacific Ocean, as far as Peru[6], and atmospheric shockwaves that propagated around the globe[4,7,8]. Based on stereoscopic geostationary satellite observations, the overshooting top of the plume was observed at altitudes over 50 km, a record in the satellite era[9]. Volcanic ash, gas and water vapour were injected well into the stratosphere, with a small part of the plume reaching the lower mesosphere[10]. Although the explosivity of the eruption was unprecedented, best estimates from different satellite instruments are consistent in measuring a total burden of the injected sulphur dioxide ($SO_2$) of about 0.4 Tg[11]. This is far less than the injected mass for the large magnitude Pinatubo eruption (Philippines, 1991), which emitted 14 to 23 Tg of $SO_2$[12], or even the more recent moderate stratospheric Raikoke 2019 (1.5 ± 0.2 Tg[13]) or Nabro 2011 eruptions (1.6 Tg[14]). Based on this modest emission of $SO_2$, it was initially suggested that the impact of HT on the stratospheric aerosol layer and climate is negligible (http://www.sparc-ssirc.org/downloads/VolRes_summary_of_the_Hunga-Vfinal.pdf).

In contrast to the expectation from the modest stratospheric $SO_2$ emission, we show that the HT eruption of 15th January 2022 produced exceptionally large stratospheric aerosol and water vapour perturbations, that in turn have produced substantial effects on the atmospheric radiation budget, with significant impacts on the plume vertical displacement and dispersion, and on the climate system.

## Results and discussion

**Initial dispersion, evolution and optical properties of the HT aerosol plume**. With the high spatial and temporal resolution monitoring capability from geostationary satellite instruments (Himawari Ash RGB product, see Methods), variations in the volcanic plume structure during the initial days after the HT eruption can be observed (Fig. 1). The HT volcano violently erupted on 15th January, with a number of distinct explosive episodes beginning at 04:15 UTC[4,5]. A volcanic umbrella formed during the first hours after the eruption, representing a combined signal across this extremely explosive phase. At this stage, the localised plume is dominated by ash and water condensates (liquid water and ice crystals), visible as a black-brownish spot in Fig. 1a. A sulphur-rich plume gradually separates on the western side, sometime after 19:00 on 15th January. While the ash/ice component stays local and gradually dissipates, likely due to sedimentation (brownish-black plume in Fig. 1b), the sulphur-rich plume's component is advected towards the west (greenish plume in Fig. 1b). Notice the absence of red, reddish or yellow colours that would indicate a thin ash plume or a mixture of ash and sulphur compounds. Over 16th-18th January, the sulphur-dominated plume moves across Australia and then towards the southern Indian Ocean (Fig. 1c). We stress that this satellite product cannot distinguish between $SO_2$ and sulfate aerosols, which have overlapping spectral signatures in this spectral range and both appear as green[15]. However, by comparing these Ash RGB Himawari images with IMS/IASI mapping of SO2 and sulfate-specific aerosol optical depth (AOD) (see Methods and more details in Ref. 16), we show that most of the greenish plume observed in Fig. 1 is composed of secondary sulfate aerosols rather than $SO_2$. This hints that an exceptionally rapid conversion of volcanic $SO_2$ emissions to secondary sulfate aerosols may have occurred, which could potentially explain why the retrieved total $SO_2$ emitted mass is relatively low, while the stratospheric aerosol perturbation is high. One reason for the rapid conversion of $SO_2$ to secondary sulfate aerosols may have been the extensive availability of water vapour (see Section "The water vapour plume" and Refs. 10, 17). The rate of $SO_2$-to-aerosol conversion, at stratospheric temperature conditions, depends strongly on the relative humidity, a higher humidity generating a faster rate of new sulfate aerosol particle formation[18].

High vertical resolution observations with the satellite-borne LiDAR CALIOP (see Methods) confirm this initial evolution of the HT aerosol plume. A first overpass on 15th January reveals the presence of aspherical particles within the plume (Fig. S1), i.e., ash and/or ice crystals, at altitudes between 34 km and the

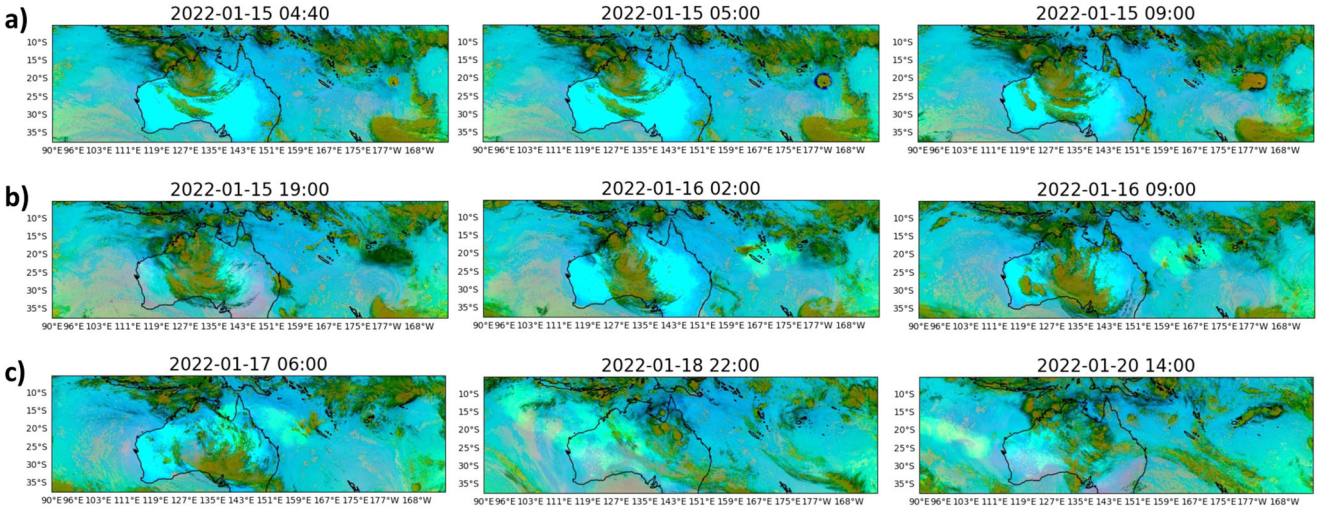


**Fig. 1 Volcanic injection and initial HT plume evolution.** Selected Ash RGB Himawari images for three sequences of the initial dispersion of the HT volcanic plume (15th January at 4:40 to 20th January at 14:00). **a** HT explosion and plume rise; **b** disappearing ash/ice signal; **c** sulphur-rich plume dispersion across Australia. All times are UTC. By a RGB band combination, this product allows to qualitatively distinguish thick ash plumes or ice clouds (brown), thin ice clouds (dark blue) and sulphur-containing plumes (green). Mixed ash/sulphur-containing volcanic species would appear in reddish and yellow shades.

maximum range of CALIOP observations at 40 km. At this stage, relatively large $SO_2$ content (5–10 Dobson Units) is observed by IMS/IASI, with concurrent low sulfate-specific AOD (<0.04). A relatively large total AOD is observed by the plume-localised CALIOP observations (0.26 at 532 nm) and by the stratospheric-integrated OMPS-LP AOD (SAOD, see Methods) satellite observations (~0.2 at 675 nm), suggesting that a majority of the AOD may come from non-sulfate aerosols. The situation is very different for the CALIOP overpass of the following day, 16th January (Fig. 2). By then, the depolarisation is already as low as 2% (with larger values only at the bottom of the plume), suggesting an increasing presence of spherical particles. This variation could be due to either ash/ice particles removal by sedimentation (at super-micron sizes) and/or due to rapid formation of secondary sulfate aerosols. The occurrence of the latter process is also indicated by an increase in IMS/IASI sulfate-specific AOD (~0.1 in the leading edge of the plume, see Fig. 2b). Exceptionally large AOD values of almost 0.5 in the visible spectral range are observed by CALIOP during plume intercepts on 16th January and the following few days. This can almost entirely be attributed to sulfate aerosols.

Ground-based aerosol sun-photometer observations from the AERONET network (see Methods) confirm the overpass of the plume in Australia and beyond, and an evolution towards small and reflective (single scattering albedo ~ 0.98 at 440 nm) sulfate aerosols, during this initial dispersion phase (Fig. S2). The overpass of a plume dominated by fine aerosols is observed over eastern Australia (Lucinda AERONET station, 18.5°S 146.4°E) starting on 16th January and then, 2 days later, over western Australia (Learmonth AERONET station, 22.2°S 114.1°E), with fine-mode-specific AOD in the range 0.5–1.0 at ~500 nm. The evolution observed from the ground is consistent with satellite observations, i.e., Himawari timing and CALIOP aerosol burden. Observations from IMS/IASI show that the plume is quickly transported westward over the Indian Ocean and a corresponding increase in fine mode AOD is observed from the ground at La Réunion island (Réunion Saint Denis and Maïdo OPAR AERONET stations, 20.9°S 55.5°E and 21.1°S 55.4°E, respectively) starting from 22nd January, with slightly reduced AODs (peak value ~0.6) due to plume dilution. A rapid-response balloon campaign was carried out at La Réunion to observe the young dispersed HT plume and to characterise its microphysical state[19]. In situ LOAC aerosol optical observations (see Methods) show enhanced aerosol extinction values at around 22 and 25 km altitude, composed of submicron, mainly liquid aerosol particles (Fig. S3).

Over the following weeks, the HT plume was quickly advected zonally across the globe by the prevailing easterly winds, circumnavigated the Earth and was observed again in northern Australia at the end of January 2022. The dynamics linked to the dispersion of the HT plume during the first 6 months after the main eruption is described further in Ref. 16. Peak optical depths of ~0.2 are systematically observed by CALIOP, e.g., on 8th February (Fig. S4), with very low depolarisation ratio (<2%), indicating that the dispersed plume is dominated by spherical sulfate aerosols. Relatively small colour ratio might indicate an increase in aerosol size, likely mainly due to sulfate aerosols water uptake/coagulation processes.

**Impact on the global stratospheric aerosol layer**. Using the information content in long time series of different satellite observations, insights into the HT plume longer-term evolution (weeks to months timescale) and the comparison of its impact with recent stratospheric eruptions can be obtained. A clear but limited enhancement of $SO_2$, with respect to background $SO_2$ levels, is apparent from zonal average IMS/IASI $SO_2$ observations (Fig. 3a). Using this dataset, the $SO_2$ burden associated with the main eruption of 15th January is estimated at 0.5 Tg immediately after the eruption, consistently with estimates in Ref. 11. Nevertheless, the $SO_2$ burden increases in the few following days and reaches values of about 1.0 Tg on 18th January. This might point at an underestimation of the initial $SO_2$ burdens possibly associated with instrumental saturation and/or the opacity of the very early plume due to ash/ice content. The sulfate aerosol plume starts to form very fast after the eruption, with an enhancement already visible on January 16th (zonal average sulfate-specific AOD in Fig. 3b). The $SO_2$ e-folding time is about 15 days, which suggests a 2–3 times faster $SO_2$-to-sulfates conversion rate than expected at these altitudes[20] and is consistent with the water-vapour-enhanced conversion discussed in Ref. 21. The sulfate aerosol formation is very sustained and the sulfate-specific AOD zonal averages quickly reach values as large as 0.01. This is a large value because: (1) it is zonally averaged over the whole globe and (2) IMS/IASI sulfate-specific AOD retrievals are in the mid-infrared, which translates into much larger sulfate-specific AOD values in the visible spectral range. Two different plume branches can be observed (Fig. 3a–c) a northern branch, with slower sulfate aerosol formation and a southern branch, with quicker sulfate aerosol formation and a rapid consumption of $SO_2$. Overall, the HT plume dispersed quickly over the global southern hemispheric tropics and limited parts of the plume crossed the equator, enhancing the stratospheric aerosol layer also in the Northern Hemisphere. This is a quite singular dispersion dynamics compared to recent stratospheric events, whose dispersion was largely poleward[22,23]. The relatively fast HT plume cross-equatorial dispersion might be due to the particularly high altitude of the injection for this eruption[24].

Time series of OMPS-LP SAOD show that the HT eruption has produced the largest peak SAOD perturbation during its OMPS mission (Fig. 3d), larger than, e.g., the Raikoke eruption 2019[23] and the Australian fires 2019–2020[25]. The mean impact on the tropical and Southern Hemispheric stratosphere, as well as on the global stratosphere, is the largest observed by OMPS-LP (global average: ~0.02, about two times larger than the Australian fires 2019–2020 impact; Southern Hemispheric average: ~0.03, two to three times larger than the Australian fires 2019–2020 impact, tropical average: ~0.03, at least three times larger than any post-Pinatubo stratospheric event) (Fig. 3e,f). The Northern Hemispheric SAOD impact of HT eruption is more limited and similar to what observed after the Raikoke eruption in 2019. While Australian fires 2019–2020 was previously considered the largest SAOD perturbation since Pinatubo eruption in 1991[23,25], our results show that the impact of the HT eruption on the stratospheric aerosol layer is the strongest since Pinatubo 1991. The impact of HT eruption on the stratospheric aerosol layer is at least five times larger than what initially proposed shortly after the eruption (i.e., a global SAOD perturbation of 0.0055 at 550 nm estimated with the EVA_H model[26], see http://www.sparc-ssirc.org/downloads/VolRes_summary_of_the_Hunga-Vfinal.pdf). The tropical and Southern Hemispheric impacts of the HT eruption were particularly strong and with magnitude comparable to the impact of El Chichon eruption in 1982 (Fig. 3f). Based on IASI/IMS observations, the sulfate aerosol total mass burden, during these initial dispersion phases, reaches values between 1.0 and 3.0 Tg at the beginning of February 2022.

**The water vapour plume**. The underwater HT eruption injected a huge amount of water vapour into the stratosphere, with an estimated amount exceeding 100 Tg[10,17]. These water vapour emissions are unprecedented in the satellite era; nevertheless,

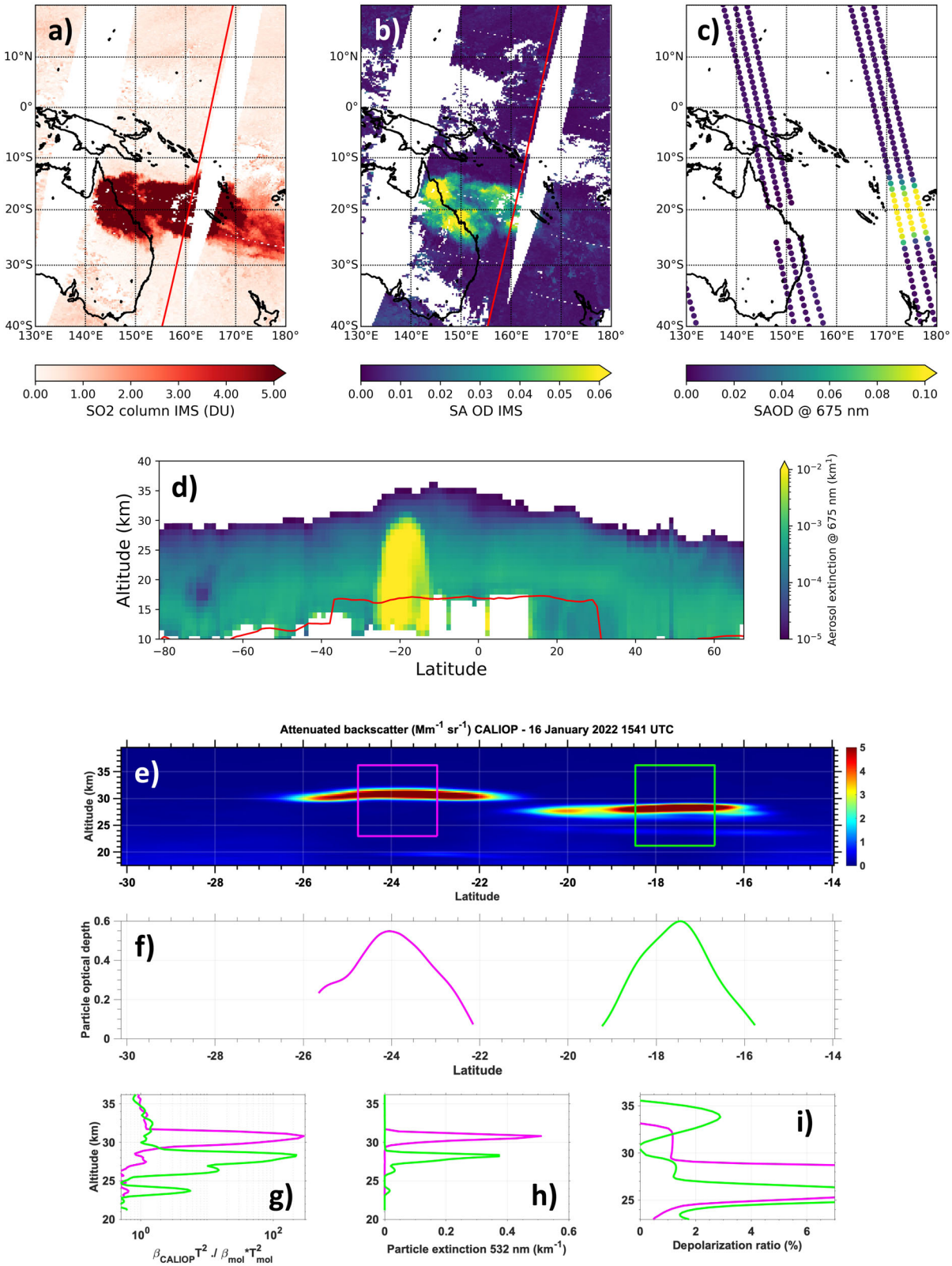


**Fig. 2 The physicochemical properties of the early HT plume.** IMS/IASI $SO_2$ (**a**) and sulfate-specific AOD (**b**) observations for 16th January at 23:07 UTC. **a**, **b** the red line is CALIOP track for the same day at 15:41 UTC. OMPS-LP integrated SAOD (**c**) and vertical aerosol extinction profile (central detector, **d**) for 16th January at 2:03 and 3:27 UTC. **d** the red line is tropopause height. Attenuated CALIOP backscatter at 532 nm (**e**), and integrated in-plume AOD (**f**), corrected transmission (**g**) extinction (**h**) and depolarisation (**i**) in the two identified plumes sections (pink and green squares). The CALIOP track of **e**–**i** is the one identified in **a** and **b**. Due to the time mismatch between CALIOP and IASI orbits, the CALIOP trace actually crossed both the eastern part of the aerosol plume in **a**, **b** (lower plume at 27 km) and the western part (upper plume at 30 km) which has already reached Australia in the display.

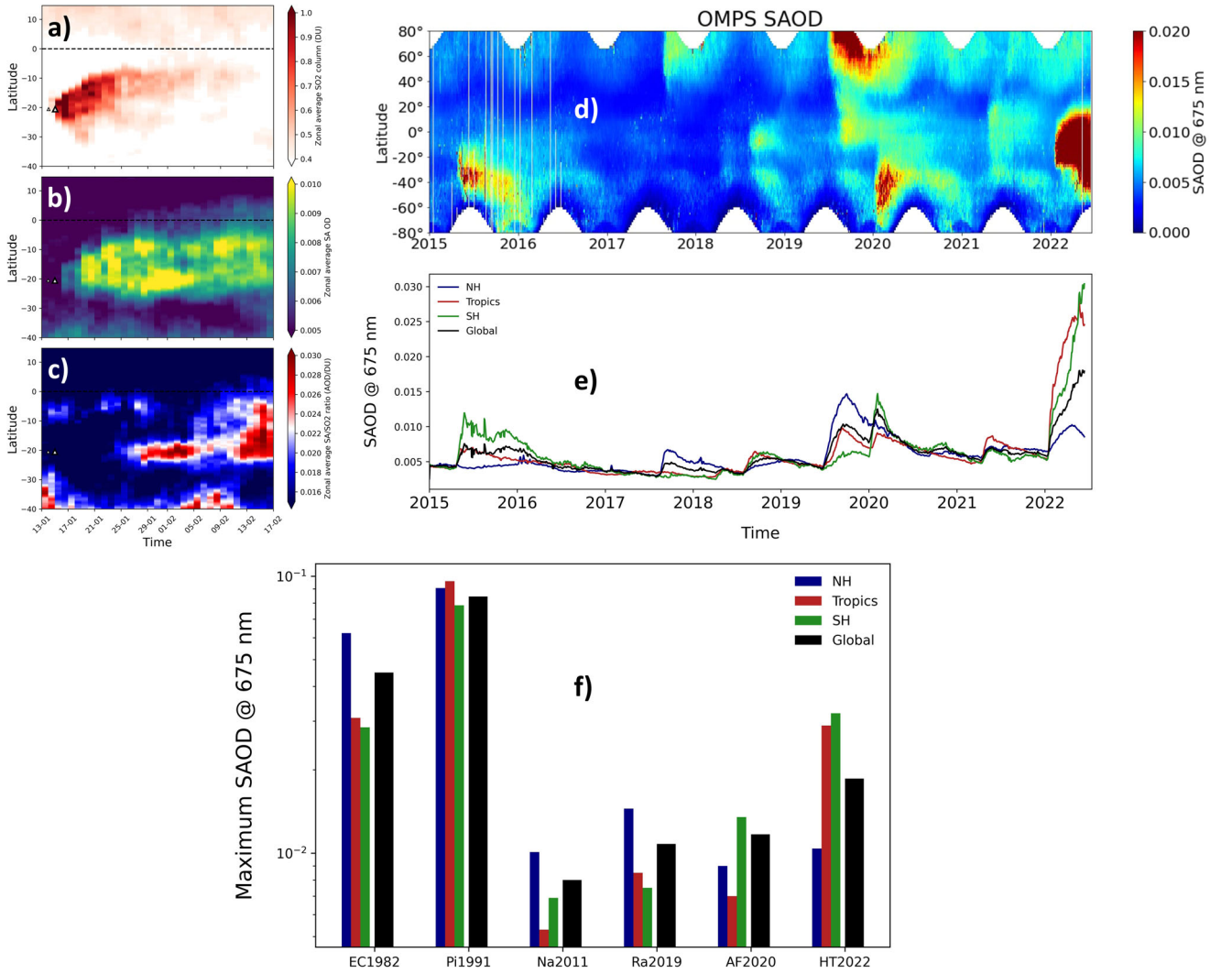


**Fig. 3 Longer-term HT plume evolution and its comparison with recent past events.** Zonal average IMS/IASI $SO_2$ observations (**a**), sulfate-specific AOD (**b**) and their ratio (**c**), for the first month of HT plume dispersion. Black triangles in **a**–**c** indicate the main HT eruption of January 15th (large triangle) and the previous smaller event of January 14th (that had a small but visible impact on the $SO_2$ distributions). Time series of the OMPS-LP zonal average SAOD (**d**) and tropical (Tropics: 30°N–30°S, red line), Northern Hemisphere (NH: 0–80°N, blue line), Southern Hemisphere (SH: 0–80°S, green line) and global (Global: 80°N–80°S, black line) SAOD (**e**). The OMPS-LP time series are updated to 15th June 2022. Global, Tropical, Northern Hemispheric and Southern Hemispheric peak SAOD values for the stratospheric events: HT eruption in 2022 (HT2022), Australian fires in 2019-2020 (AF2020), Raikoke eruption in 2019 (Ra2019), Nabro eruption in 2011 (Na2011), from OMPS-LP observations, and Pinatubo eruption in 1991 (Pi1991) and El Chichon eruption in 1982 (EC1982), from the GloSSAC database (**f**).

estimates with petrological methods indicate that large eruptions of the past, including the one of Pinatubo in 1991, may have produced even significantly larger water vapour emissions[11]. The large HT water vapour emissions are likely due to both volcanic caldera intrusion of seawater and mechanical interaction with seawater, over the underwater eruptive crater, during the eruption. As a result, record-breaking water vapour content is found in the stratosphere, within the plume, with radio-soundings (see Methods). Water vapour concentrations exceed 0.5–0.8 molecules $cm^{-3}$ (up to over 1500 ppmv) for the fresh plume over Australia on January 19–20th, 0.4 molecules $cm^{-3}$ (~500 ppmv) for the dispersed plume at Saint Helena Island on January 25th, and 0.1 molecules $cm^{-3}$ (~100 ppmv) after a full circumnavigation of the Earth, back over Australia on 8th February (Fig. 4a).

**Radiative impacts of the aerosol and water vapour plume.** Localised stratospheric radiative heating/cooling due to aerosol and water vapour perturbation from the HT plume are calculated with offline radiative transfer (RT) modelling (see Methods). Three plume-perturbed cases are considered, using CALIOP LiDAR-derived aerosol extinction: (1) fresh plume, higher section (average aerosol extinction in the pink box of Fig. 2, 16th January overpass); (2) fresh plume, lower section (average aerosol extinction in the green box of Fig. 2, January 16th overpass); (3) aged plume, after a full global zonal circumnavigation (average aerosol extinction in the green box of Fig. S4, 8th February overpass). Based on the plume evolution discussed above, aerosol layers are simulated as small and very-weakly-absorbing (to account for a possible very small residual ash fraction) sulfate particles, for the fresh plume, with a small increase in size due to condensation/coagulation and purely scattering sulfate aerosols, for the aged plume. Corresponding water vapour perturbations are obtained with radio-sounding observations in western Australia of Fig. 4a (fresh plume, higher section, 19th January; fresh plume, lower section, 20th January; aged plume, 8th February). An additional case is considered for water vapour perturbations

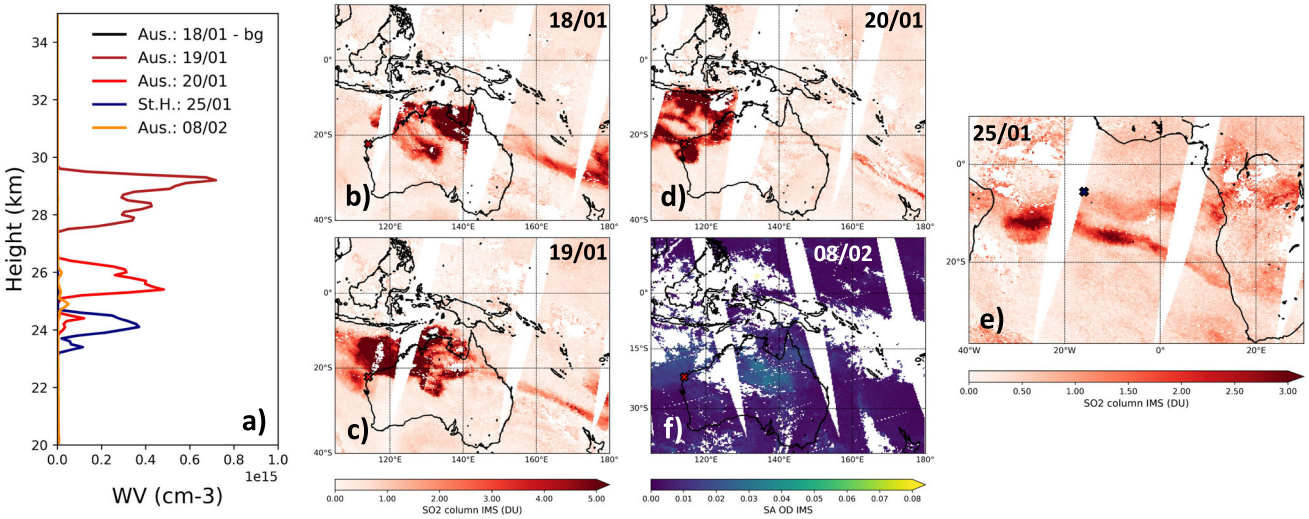


**Fig. 4 Water vapour in the HT plume.** Water vapour radio-sounding observations over western Australia on 18th January (unperturbed background in RF estimations, black line), 19th (dark red line), 20th (red line), and 8th February (yellow line), and over Saint Helena island (blue line) (**a**). Plume and sounding positions (red crosses) are shown in **b**–**f**, using IMS/IASI $SO_2$ and sulfate-specific AOD observations.

**Table 1 Short-term RF of the HT plume.**

| | | Fresh plume, higher section | Fresh plume, lower section | Aged plume |
|---|---|---|---|---|
| TOA | A (Aerosol) | −19.4 | −12.1 | −0.6 |
| | WV (Water vapour) | −0.7 | −0.4 | +0.8 |
| | A + WV (Aerosol + Water vapour) | −20.1 | −12.5 | +0.2 |
| Surface | A (Aerosol) | −27.9 | −17.5 | −1.7 |
| | WV (Water vapour) | 0.0003 | 0.0006 | 0.0018 |
| | A + WV (Aerosol + Water vapour) | −27.9 | −17.5 | −1.7 |

TOA and surface RF for the aerosol (A) and water vapour (WV) plumes, and both (A + WV), for the three cases described in Fig. 5 caption. The LW and SW RFs are added up in the table. All RF values are in $Wm^{-2}$.

in the southern Atlantic Ocean, observations at Saint Helena island of January 25th (see Fig. 4a). Even if the aerosol and water vapour plumes are not sampled at exactly the same location and time, these are representative of the initial plume state and evolution (fresh or aged, after one full Earth circumnavigation), as well as their different sections (higher and lower, for the fresh plume). The plume's localised aerosol shortwave (SW) radiative heating and longwave (LW) radiative cooling compensate to a large extent, the local net aerosol radiative effect being near-zero heating rates (Fig. 5a). For the higher section of the fresh plume, the water vapour LW cooling dominates the localised stratospheric heating/cooling rates (Fig. 5b). This produces a very large total plume cooling rate for the higher sections of the fresh plume, reaching values as large as −10 K/d (Fig. 5c). For the lower section of the fresh plume, this cooling is smaller, due to the weaker radiative impact of water vapour at lower altitudes; this sums up to a small positive aerosol's heating rate to produce a near-zero total plume heating rate. For the aged plume, both aerosol and water vapour heating/cooling rates are very small due to progressive dilution. The very large cooling rate for the higher section of the fresh plume has produced a rapid descent of this part of the plume, which is estimated at 11.3 K/d in potential temperature from CALIOP during the first week of February and falls to 3.6 K/d during the following weeks due to dilution (Fig. 5d). This radiative cooling is a major forcing for the initial vertical dynamics of the HT plume and its subsequent atmospheric dispersion. This radiatively-driven vertical dynamical feature contrasts with the usual ascent observed in young volcanic clouds due to radiation absorption from volcanic aerosol and $SO_2$ emissions[27]. This reflects the unusually large amount of water vapour emissions of HT. The top-of-atmosphere (TOA) and surface radiative forcing (RF) of the plume is also estimated, by considering again the fresh and aged plume cases introduced above and both aerosol and water vapour effects (Table 1 and Fig. S5). For the fresh plume, the SW and LW aerosol components dominate, producing large instantaneous local RF reaching values of $-20\,Wm^{-2}$ (TOA) and $-28\,Wm^{-2}$ (surface), for the higher section. The aerosol RF component fades rapidly for the aged plume, due to dispersion/dilution. By contrast, the LW and SW water vapour RF switches from negative to positive values (due to its descent in altitude) and dominates at TOA for the aged plume. At this dispersion stage, the aerosol plume is relatively homogeneous in the approximate latitude range 10°N-30°S, so this RF estimate, though not an hemispheric average, is representative of this full latitude band. Thus, contrary to what was observed for all the stratospheric volcanic eruptions of the last 30 years, the HT plume might produce a slightly positive TOA RF, with a subsequent small warming effect of the climate system. The surface RF of the aged plume remains dominated by aerosols and reaches negative values as large as almost $-2\,Wm^{-2}$, which is quite large if compared with recent events. As a point of comparison, the Raikoke eruption in 2019 and Australian fires 2019–2020 have hemispheric surface RF of about $-0.8\,Wm^{-2}$ (Ref. 15) and $-2.0\,Wm^{-2}$ (Ref. 16), respectively.

The large perturbations of the aerosol and water vapour contents in the stratosphere from the HT eruption are expected to

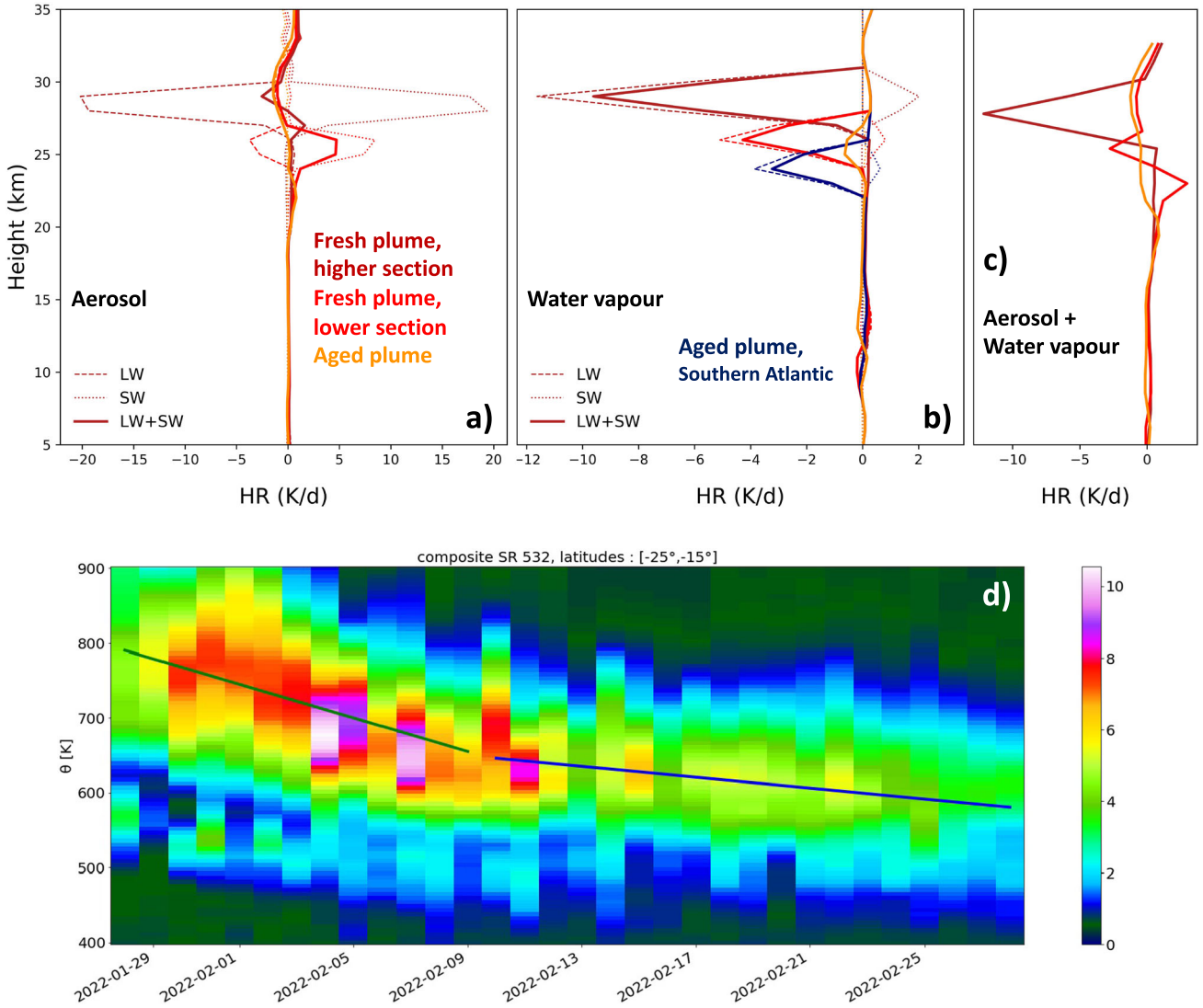


**Fig. 5 Stratospheric radiative cooling due to the HT plume and plume descent.** Aerosol (**a**), water vapour (**b**) and total plume (**c**) LW (dashed lines), SW (dotted lines) and total (solid lines) radiative heating rates (HR) for the basic cases discussed in the text: fresh plume, higher section (dark red), fresh plume, lower section (red) and aged plume (orange). The additional case of the southern Atlantic profile is presented for water vapour only in **b** (blue). The CALIOP aerosol observations and water vapour radio-sounding, even if representative of the same plume sections, are taken at different time intervals (radio-soundings are taken 2 days later than CALIOP overpasses of the early plume), thus CALIOP profiles are vertically shifted to match the water vapour enhancements observed with radio-sounding. CALIOP 532 nm attenuated backscatter ratio (SR) averaged daily over all night traces in the zonal direction and between 15°S and 25°S in latitude (**d**). The fit is performed over all pixels where SR > 4 and for the two periods Jan 28–Feb 09 (green line, −11.3 K/d) and Feb 10–28 (blue line, −3.6 K/d).

produce significant impacts on the stratospheric ozone layer, at longer time scales[21]. The likely stratospheric ozone depletion due to aerosol and water vapour injections might produce a large additional cooling of the stratosphere and negative TOA and surface radiative forcing. A negative stratospheric temperature anomaly is observed, at longer timescales, with satellite observations and attributed to the Hunga Tonga effect in Ref. 28. Nevertheless, at the timescales of this study, no stratospheric ozone reduction is observed and thus its radiative effect is not addressed here. Due to the likely TOA warming and stratospheric cooling, this eruption falls outside the range of magnitude categorisation of the recent VCI (Volcano-Climate Index)[29]. We suggest that VCI and other similar parameters be modified to include uncommon events, like Hunga Tonga and phreato-Plinian eruptions in general.

These estimations of the radiative impacts of the HT eruption, here obtained for specific stages of the initial plume dispersion, pave the way to more systematic modelling studies, to confirm the peculiar nature of this event and study its evolution at longer time scales.

## Conclusions

The phreato-Plinian HT eruption of 15th January 2022 produced the largest global perturbation of stratospheric aerosols since the Pinatubo eruption in 1991 and the largest perturbation of stratospheric water vapour observed in the satellite era. A total burden of 1.0 to 3.0 Tg of sulfate aerosols was injected into the stratosphere by this event. Particularly strong tropical and Southern Hemispheric impacts on the stratospheric aerosol optical depth place this event on par with the impacts of El Chichon eruption in 1982 in the same latitude bands. The extremely large water vapour availability (more than 100 Tg of water vapour were injected in the stratosphere during the event) was the possible reason for the observed rapid conversion of

volcanic $SO_2$ emissions to secondary sulfate aerosols. The large stratospheric water vapour perturbation associated with the HT eruption had also a fundamental role in the plume's radiative impacts during the first weeks after the eruption, causing a fast radiatively-driven plume descent and a warming effect on the climate system. These very peculiar radiative impacts, as well as the long-term impacts of the HT eruption on the stratospheric composition, must be followed and confirmed during the next months with further studies.

## Methods

**Volcanic plume tracking with geostationary satellite imagers**. In order to track, with high temporal and spatial resolution, the early stages of the evolution of the plume, we use a composite RGB product that benefits from the sensitivity of the Himawari-8 8.5 µm band to $SO_2$ and sulfate aerosols. The product is based on the EUMETSAT Ash RGB recipe and uses the brightness temperatures (BT in K) of the three channels: 8.5, 10.4 and 12.3 µm. The recipe for the three colour indexes ranging from 0 to 1 is R = (BT(12.3) - BT(10.4) + 4)/6, G = (BT(10.4) - BT(0.85) +4)/9, B = (BT(10.4) - 243)/60.

**Volcanic sulphur dioxide and sulfate aerosols satellite observations with the IMS scheme**. The RAL (Rutherford Appleton Laboratory) Infra-red/Microwave Sounder (IMS) retrieval core scheme[30] uses an optimal estimation (OE) spectral fitting procedure to retrieve atmospheric and surface parameters jointly from co-located measurements by IASI (Infrared Atmospheric Sounding Interferometer), AMSU (Advanced Microwave Sounding Unit) and MHS (Microwave Humidity Sounder) on MetOp spacecraft series, using RTTOV 12 (Radiative Transfer for TOVS) as the forward radiative transfer model. The use of RTTOV12 enables the quantitative retrieval of volcanic-specific aerosols (sulfate aerosol) and trace gases ($SO_2$). The present paper uses IMS $SO_2$ and sulfate aerosols observations from its near-real time implementation (images can be viewed here: http://rsg.rl.ac.uk/vistool). The IMS scheme retrieves the $SO_2$ in the sensitive region around ~1100–1200 $cm^{-1}$ (Ref. 14). It retrieves sulfate-specific AOD (Aerosol Optical Depth) at ~1200 $cm^{-1}$ (the peak of the mid-infrared extinction cross section[31]), assuming a Gaussian extinction coefficient profile shape peaking at 20 km altitude, with 2 km full-width-half-maximum. The bulk of the spectroscopic information on $SO_2$ and sulfate aerosols, in the IMS scheme, thus comes from the IASI Fourier transform spectrometer, thus we refer to these observations as IMS/IASI. The total mass burden of $SO_2$ and sulfate aerosol from HT eruption are obtained with IMS/IASI observations, considering the latitude interval between the equator and 40°S and by subtracting a baseline burden before the eruption (on 13th January). For the sulfate aerosol mass burden, hypotheses are made on the mass aerosol extinction efficiency (MEE), which depends critically on the particles mean size. Extreme values of 0.15 (typical for mean size smaller than about 0.5 µm) and 0.4 $m^2/g$ (typical for mean size larger than about 0.5 µm) have been considered for the mid-infrared MEE.

**Volcanic plumes observations with the CALIPSO-CALIOP space LiDAR**. We use attenuated backscatter profiles at 532 nm measured by the CALIOP (Cloud-Aerosol Lidar with Orthogonal Polarisation) spaceborne LiDAR[32] onboard the CALIPSO (Cloud-Aerosol Lidar and Infrared Pathfinder Satellite Observation) satellite to derive optical properties of the volcanic aerosol plumes. Their AOD is estimated from the ratio of the LiDAR signal at aerosol-free altitudes above and below the volcanic plumes. Aerosol LiDAR ratios are roughly calculated by dividing the AODs by the vertically integrating attenuated backscatter after subtracting molecular backscatter. Finally, LiDAR ratios are used for calculating aerosol extinction profiles using a classic equation[33].

**Volcanic plumes observations with the OMPS Limb Sounder**. The Ozone Mapping and Profiler Suite Limb Profiler (OMPS-LP) instruments flights onboard the Suomi National Polar-orbiting Partnership (Suomi-NPP) satellite since January 2012. It observes vertical profiles of scattered solar radiation, in the 290–1000 nm spectral range, in a limb-viewing geometry, i.e., tangent to the Earth's atmosphere. We use the aerosol extinction profile inversion algorithm v2.0 (Ref. 20) at 675 nm and the integrated stratospheric AOD (SAOD). With respect to previous datasets versions, this dataset exhibits significant retrieval improvements, especially in the Southern Hemisphere (SH), when compared with independent datasets[34]. The OMPS-LP SAOD time series is extended back, to compare the HT eruption to earlier Pinatubo and El Chichon eruption, using the GloSSAC (Global Space-based Stratospheric Aerosol Climatology) database v2.0[35].

**In situ measurements of volcanic aerosol size distributions with LOAC**. The Light Optical Aerosol Counter (LOAC) is a multi-angle in situ optical particle[36] which, thanks to its very limited weight (~300 g), has been operated on small balloon measurement flights at the Observatoire de l'atmosphère du Maïdo at La Réunion island (21.1 S, 55.3E), after the HT eruption. Using a laser at 650 nm wavelength, aerosol concentration is derived with LOAC for particles between 150 nm and 30 µm, in 19 size classes. The aerosol extinction is also estimated. For more details please refer to Ref. 19. In this work, we show LOAC measurement for 23 January 2022 (20-21:30 UTC).

**Multi-station analysis of ground-based AERONET sunphotometric data**. A multi-station analysis of L1.5 cloud-screened and quality assured sunphotometric data from the AERONET (AErosol RObotic NETwork)[37] is carried out at stations in Australia and La Réunion Island, using the VolcPlume portal for the 4D multi-scale monitoring and analysis of volcanic plumes. The contribution with time of the fine (sub-micron) and coarse (super-micron) modes to the total AOD at 500 nm, derived from the spectral deconvolution algorithm[38], is analysed to detect volcanic sulfate aerosols as in Ref. 39.

**Water vapour observations with radio-sounding**. We use water vapour radio-soundings in Western Australia and Saint Helena island. Stratospheric humidity measurements with standard meteorological radio-sounds are particularly challenging due to the low relative humidity and outgassing from the balloon envelope[40] which typically contaminates the measurement by tenths of ppmv up to ~100 ppmv at 30 km. However, the exceptionally large relative humidity values found in the HT plume outweigh contamination and uncertainties of Vaisala RS41 radio-sondes used in this work, and the ultra-moist plume clearly stands out of background variability in those soundings. The unusually humid upper stratosphere and its high temperature turn out to be a favourable environment for such measurements. For water vapour sensitive radiative calculations, we remove the systematic impact of sonde outgassing by computing an anomaly with respect to the 90% quantile radio-sonde profile over one month and adding it to a background profile deduced from satellite measurements by Aura MLS.

**Radiative forcing and heating/cooling rates modelling with the LibRadtran suite**. The clear-sky equinox-equivalent daily-average shortwave (SW, integrated between 300 and 3000 nm) and longwave (LW, integrated between 2.5 and 100 µm) surface and top of the atmosphere (TOA) direct radiative forcing (RF) are estimated using the UVSPEC (UltraViolet SPECtrum) radiative transfer model in the libRadtran (library for Radiative transfer) implementation[41] and the offline modelling methodology described in Refs. 25 and 42. The SW and LW radiative heating rates are also estimated with UVSPEC/libRadtran, for the same scenarios. Independent cases to account for water vapour and aerosol perturbations associated with the HT eruption are considered. Baseline simulations are obtained with an unperturbed water vapour sounding (over Western Australia on 18 January 2022, briefly before the HT plume overpass, see Fig. 4b) and a standard background aerosol profile (Shettle standard in Ref. 43). Volcanic-perturbed simulations are obtained with in-plume water vapour radio-sounding observations and CALIOP aerosol extinction observations, for both fresh (16–20th January) and aged plume (8th February). More details of water vapour and aerosol observations used as inputs for the offline radiative transfer modelling are in the Section "Radiative impacts of the aerosol and water vapour plume". The spectral variability of the aerosol extinction, and the absorption and angular scattering properties of the aerosol plume are based on hypotheses detailed in the Section "Radiative impacts of the aerosol and water vapour plume". The atmospheric conditions for all simulations are based on the AFGL (Air Force Geophysical Laboratory) standard tropical atmosphere[44].

## Data availability

The OMPS-LP data are freely available from EarthData centre at: https://disc.gsfc.nasa.gov/datasets/OMPS_NPP_LP_L2_AER_DAILY_2/summary. The CALIOP data v3.41freely are available from the NASA LARC website at: https://doi.org/10.5067/CALIOP/CALIPSO/CAL_LID_L1-VALSTAGE1-V3-41. The Himawari observations are freely available from the AERIS-ICARE data centre, at the following link: https://www.icare.univ-lille.fr/asd-content/browse/geoview. The IMS/IASI SO2 and SA OD datasets used in this work can be accessed for the following data record: https://doi.org/10.5281/zenodo.7102472. The LOAC in situ observations can be accessed from the following data record: https://zenodo.org/record/6522689#.YrBjAd869hE. The AERONET data are freely available at the following website: http://aeronet.gsfc.nasa.gov and the datasets used in the present study can be downloaded via the VolcPlume portal at the following link: https://doi.org/10.25326/362. Radio-sounding observations are freely available at the following link: http://www.weather.uwyo.edu/upperair/bufrraob.shtml.

## Code availability

A python package to read and process the IMS/IASI data is available at the following link: https://github.com/bernard-legras/ASTuS/tree/master/IMS and in the IMS-reader.tgz archive at the following link: https://doi.org/10.5281/zenodo.7102472. The LibRadtran software can be freely downloaded at the following link: http://www.libradtran.org/doku.php?id=download.

Received: 5 May 2022; Accepted: 8 November 2022;
Published online: 19 November 2022

## References


1. Solomon, S. et al. The persistently variable background stratospheric aerosol layer and global climate change. *Science* **333**(6044), 866–870 (2011).
2. Andersson, S. et al. Significant radiative impact of volcanic aerosol in the lowermost stratosphere. *Nat. Commun.* **6**, 7692 (2015).
3. Marshall, L. R. et al. Volcanic effects on climate: recent advances and future avenues. *Bull. Volcanol.* **84**, 54 (2022).
4. Podglajen, A. et al. Stratospheric balloon observations of infrasound waves from the January 15 2022 Hunga eruption, Tonga. *Geophys. Res. Lett.* **49**, e2022GL100833 (2022).
5. Astafyeva, E. et al. The 15 January 2022 Hunga Tonga eruption history as inferred from ionospheric observations. *Geophys. Res. Lett.* **49**, e2022GL098827 (2022).
6. Lynett, P. et al. Diverse tsunamigenesis triggered by the Hunga Tonga-Hunga Ha'apai eruption. *Nature* **609**, 728–733 (2022).
7. Amores, A. et al. Numerical simulation of atmospheric Lamb waves generated by the 2022 Hunga-Tonga volcanic eruption. *Geophys. Res. Lett.* **49**, e2022GL098240 (2022).
8. Wright, C. J. et al. Surface-to-space atmospheric waves from Hunga Tonga–Hunga Ha'apai eruption. *Nature* **609**, 741–746, https://doi.org/10.1038/s41586-022-05012-5 (2022).
9. Carr, J. L., Horváth, Á., Wu, D. L. & Friberg, M. D. Stereo plume height and motion retrievals for the record-setting Hunga Tonga-Hunga Ha'apai eruption of 15 January 2022. *Geophys. Res. Lett.* **49**, e2022GL098131 (2022).
10. Khaykin, S. et al. Global perturbation of stratospheric water and aerosol burden by Hunga eruption, *Earth and Space Science Open Archive* [preprint], https://doi.org/10.1002/essoar.10511923.1 (2022).
11. Carn, S., Krotkov, N., Fisher, B. & Li, C. Out of the blue: volcanic SO2 emissions during the 2021-2022 eruptions of Hunga Tonga - Hunga Ha'apai (Tonga). *Front. Earth Sci.* **10**, https://doi.org/10.3389/feart.2022.976962 (2022).
12. Guo, S., Bluth, G. J. S., Rose, W. I., Watson, I. M. & Prata, A. J. Re-evaluation of SO2 release of the 15 June 1991 Pinatubo eruption using ultraviolet and infrared satellite sensors. *Geochem. Geophys. Geosyst.* **5**, Q04001 (2004).
13. de Leeuw, J. et al. The 2019 Raikoke volcanic eruption—Part 1: Dispersion model simulations and satellite retrievals of volcanic sulfur dioxide. *Atmos. Chem. Phys.* **21**, 10851–10879 (2021).
14. Carboni, E. et al. The vertical distribution of volcanic $SO_2$ plumes measured by IASI. *Atmos. Chem. Phys.* **16**, 4343–4367 (2016).
15. Sellitto, P., Sèze, G. & Legras, B. Secondary sulphate aerosols and cirrus clouds detection with SEVIRI during Nabro volcano eruption. *Int. J. Remote Sens.* **38**(20), 5657–5672 (2017).
16. Legras, B. et al. The evolution and dynamics of the Hunga Tonga plume in the stratosphere, *EGUsphere* [preprint], https://doi.org/10.5194/egusphere-2022-517 (2022).
17. Millán, L. et al. The Hunga Tonga-Hunga Ha'apai Hydration of the Stratosphere. *Geophys. Res. Lett.* **49**, e2022GL099381 (2022).
18. Vehkamäki, H. et al. An improved parameterization for sulfuric acid–water nucleation rates for tropospheric and stratospheric conditions. *J. Geophys. Res.* **107**(D22), 4622 (2002).
19. Kloss, C. et al. Aerosol characterization of the stratospheric plume from the volcanic eruption at Hunga Tonga 15 January 2022. *Geophys. Res. Lett.* **49**, e2022GL099394 (2022).
20. Carn, S. A., Clarisse, L. & Prata, A. J. Multi-decadal satellite measurements of global volcanic degassing. *J. Volcanol. Geotherm. Res.* **311**, 99–134 (2016).
21. Zhu, Y. et al. Perturbations in stratospheric aerosol evolution due to the water-rich plume of the 2022 Hunga-Tonga eruption. *Commun. Earth Environ.* **3**, 248 (2022).
22. Khaykin, S. et al. The 2019/20 Australian wildfires generated a persistent smoke-charged vortex rising up to 35 km altitude. *Commun. Earth Environ.* **1**, 22 (2020).
23. Kloss, C. et al. Stratospheric aerosol layer perturbation caused by the 2019 Raikoke and Ulawun eruptions and their radiative forcing. *Atmos. Chem. Phys.* **21**, 535–560 (2021).
24. Marshall, L. et al. Exploring how eruption source parameters affect volcanic radiative forcing using statistical emulation. *J. Geophys. Res. Atmos.* **124**, 964–985 (2019).
25. Sellitto, P., Belhadji, R., Kloss, C. & Legras, B. Radiative impacts of the Australian bushfires 2019–2020 – Part 1: Large-scale radiative forcing. *Atmos. Chem. Phys.* **22**, 9299–9311 (2022).
26. Aubry, T. J., Toohey, M., Marshall, L., Schmidt, A. & Jellinek, A. M. A new volcanic stratospheric sulfate aerosol forcing emulator (EVA_H): Comparison with interactive stratospheric aerosol models. *J. Geophys. Res. Atmos.* **125**, e2019JD031303 (2020).
27. Fairlie, T. D., Vernier, J.-P., Natarajan, M. & Bedka, K. M. Dispersion of the Nabro volcanic plume and its relation to the Asian summer monsoon. *Atmos. Chem. Phys.* **14**, 7045–7057 (2014).
28. Schoeberl, M. R. et al. Analysis and impact of the Hunga Tonga-Hunga Ha'apai Stratospheric Water Vapor Plume. *Geophys. Res. Lett.* **49**, e2022GL100248 (2022).
29. Schmidt, A. & Black, B. A. Reckoning with the rocky relationship between eruption size and climate response: toward a volcano-climate index. *Ann. Rev. Earth Planet. Sci.* **50**, 627–661 (2022).
30. Siddans, R. Water Vapour Climate Change Initiative (WV_cci) - Phase One, Deliverable 2.2; Version 1.0, 27 March 2019, https://climate.esa.int/documents/1337/Water_Vapour_CCI_D2.2_ATBD_Part2-IMS_L2_product_v1.0.pdf (2019).
31. Sellitto, P. & Legras, B. Sensitivity of thermal infrared nadir instruments to the chemical and microphysical properties of UTLS secondary sulfate aerosols. *Atmos. Meas. Tech.* **9**, 115–132 (2016).
32. Winker, D. M., Hunt, W. H. & McGill, M. J. Initial performance assessment of CALIOP. *Geophys. Res. Lett.* **34**, L19803 (2007).
33. Fernald, F. G. Analysis of atmospheric lidar observations: some comments. *Appl. Opt.* **23**, 652–653 (1984).
34. Taha, G. et al. OMPS LP Version 2.0 multiwavelength aerosol extinction coefficient retrieval algorithm. *Atmos. Meas. Tech.* **14**, 1015–1036 (2021).
35. Kovilakam, M. et al. The Global Space-based Stratospheric Aerosol Climatology (version 2.0): 1979–2018. *Earth Syst. Sci. Data* **12**, 2607–2634 (2020).
36. Renard, J.-B. et al. LOAC: a small aerosol optical counter/sizer for ground-based and balloon measurements of the size distribution and nature of atmospheric particles – Part 1: Principle of measurements and instrument evaluation. *Atmos. Meas. Tech.* **9**, 1721–1742 (2016).
37. Holben, B. et al. AERONET—A federated instrument network and data archive for aerosol characterization. *Remote Sens. Environ.* **66**, 1–16 (1998).
38. O'Neill, N., Eck, T., Smirnov, A., Holben, B. & Thulasiraman, S. Spectral discrimination of coarse and fine mode optical depth. *J. Geophys. Res.-Atmos.* **108**, 4559 (2003).
39. Boichu, M. et al. Current challenges in modelling far-range air pollution induced by the 2014–2015 Bardarbunga fissure eruption (Iceland). *Atmos. Chem. Phys.* **16**, 10831–10845 (2016).
40. Vömel, H. et al. Intercomparisons of stratospheric water vapor sensors: FLASH-B and NOAA/CMDL frost point hygrometer. *J. Atmos. Oceanic Technol.* **24**, 941–952 (2007).
41. Emde, C. et al. The libRadtran software package for radiative transfer calculations (version 2.0.1). *Geosci. Model Dev.* **9**, 1647–1672 (2016).
42. Sellitto, P. et al. Synergistic use of Lagrangian dispersion and radiative transfer modelling with satellite and surface remote sensing measurements for the investigation of volcanic plumes: the Mount Etna eruption of 25–27 October 2013. *Atmos. Chem. Phys* **16**, 6841–6861 (2016).
43. Shettle, E. Models of aerosols, clouds and precipitation for atmospheric propagation studies, in: Atmospheric propagation in the UV, visible, IR and mm-region and related system aspects, no. 454 in AGARD Conference Proceedings (1989).
44. Anderson, G. P., Clough, S. A., Kneizys, F. X., Chetwynd, J. H. & Shettle, E. P. AFGL atmospheric constituent profiles (0–120 km), https://apps.dtic.mil/sti/pdfs/ADA175173.pdf (last access: 2 June 2016) (1986).


## Acknowledgements

This research has been supported by the Agence Nationale de la Recherche (grants no: 21-CE01-0007-01, ASTuS; 21-CE01-0016-01, TuRTLES; 21-CE01-0028-01, PyroStrat; 15-CE04-0003-01, VolcPlume), the Centre National d'Études Spatiales (CNES) via TOSCA/IASI grant, the Centre national de la recherche scientifique-Institut National des Sciences de l'Univers (CNRS-INSU PNTS (Programme National de Télédétection Spatiale) via MIA-SO2 grant, and the Laboratoire d'Excellence VOLTAIRE (VOLatils – Terre, Atmosphère et Interactions - Ressources et Environnement; ANR-10-LABX-100-01) and CaPPA (Chemical and Physical Properties of the Atmosphere; ANR-11-LABX-0005-01). The providers of the libRadtran suite (http://www.libradtran.org/) are gratefully acknowledged. Ghassan Taha, NASA, is gratefully acknowledged for the help with OMPS data. The AERIS thematic centre is acknowledged for the access to CALIOP and Himawari data, and for the development of the VolcPlume Portal, dedicated to the multiscale atmospheric 4D monitoring of volcanic plumes (hosted at AERIS/ICARE Data and Services), whose prototype has been initially developed within the framework of the VolcPlume ANR project (15-CE04-0003-01). M.B. acknowledges support from the European Union's Horizon Europe Framework Programme (HORIZON) FAIR-EASE (grant agreement No. 101058785) and E-shape projects. We thank the AERONET staff and site managers: V. Duflot (Univ. Réunion), I. Lau and T. Schroeder (CSIRO) for stations at La Réunion and Australia respectively.

## Author contributions

P.S. conceived the study, analysed, coordinated and interpreted the overall results; he analysed and interpreted the IMS/IASI observations, the OMPS-LP observations, generated the inputs for and run the radiative transfer modelling, and interpreted the radiative estimations. A.P. co-conceived the study, provided and interpreted the radio-sounding data, helped set up of the radiative modelling and interpreted the radiative estimations. R.B. analysed the OMPS-LP data. M.B. analysed and interpreted the AERONET sunphotometric data. E.C. provided and interpreted the IMS/IASI data. J.C. analysed the CALIOP data describing the optical and microphysical state of the plume. C.D. analysed the CALIOP data describing the fast plume descent. C.K. set up the launch of balloons carrying LOAC instruments and analysed their observations. R.S. developed and interpreted the IMS/IASI observations. N.B. set up the launch of balloons carrying LOAC instruments. L.B. contributed on the AERONET data interpretation. F.J. contributed to the LOAC launches. S.K. contributed to the interpretation of water vapour observations. J-B. R. analysed and interpreted the LOAC data. B.L. co-conceived the study, analysed the geostationary observations, supervised the CALIOP data analyses, helped set up of the radiative modelling and interpreted the radiative estimations. P.S, A.P and B.L. first noticed the unexpected nature of the radiative impacts of HT eruption.

## Competing interests

The authors declare no competing interests.

## Additional information

**Supplementary information** The online version contains supplementary material available at https://doi.org/10.1038/s43247-022-00618-z.

**Correspondence** and requests for materials should be addressed to P. Sellitto.

**Peer review information** *Communications Earth & Environment* thanks Graham Mann, Thomas Aubry and the other, anonymous, reviewer(s) for their contribution to the peer review of this work. Primary Handling Editors: Emma Liu, Joe Aslin. Peer reviewer reports are available.